Editors' Suggestion

Neutron radiography of an anisotropic drainage flow

Artem Skrypnik,[1,*] Katie Cole,[2] Tobias Lappan,[3] Pablo R. Brito-Parada,[4] Stephen J. Neethling,[4] Pavel Trtik,[5] Kerstin Eckert,[1,3] and Sascha Heitkam[1,3,†]

[1]*Institute of Process Engineering and Environmental Technology, TU Dresden, 01062 Dresden, Germany*
[2]*Department of Physics, University of Cape Town, 7700 Cape Town, South Africa*
[3]*Institute of Fluid Dynamics, Helmholtz-Zentrum Dresden-Rossendorf, 01328 Dresden, Germany*
[4]*Department of Earth Science and Engineering, Imperial College London, SW7 2AZ London, United Kingdom*
[5]*Laboratory for Neutron Scattering and Imaging, Paul Scherrer Institut, 5232 Villigen, Switzerland*

(Received 5 May 2023; accepted 8 November 2023; published 16 January 2024)

Liquid drainage through foam is dominated by gravity, capillary, and viscous forces. The liquid is conducted by an isotropic network of Plateau borders; however, imposed stress changes the alignment of the foam's structural elements. Previous numerical simulations predicted that a vertical drainage flow will be deflected horizontally if the foam is sheared. We investigated this phenomenon by measuring the distribution of the liquid fraction within a foam formed in a flat rectangular cell. The foam was subjected to shear stress under a forced liquid supply from the top of the cell. Neutron radiographies of unchanged and sheared foam were analyzed to extract measurements of the liquid fraction. Deflections in the distribution of the drainage liquid were detected and found to be positively correlated with increasing foam shear.

DOI: 10.1103/PhysRevE.109.014609

I. INTRODUCTION

Liquid foam is a heterogeneous media with distinctive mechanical properties [1,2]. It consists of gaseous bubbles contained by liquid films and liquid interstitial channels (known as Plateau borders). Under the influence of gravity and capillary forces, and counteracted by its viscosity, liquid distributes within the foam, which considerably affects the foam's structural and rheological properties. Liquid drainage through the foam is a complex process which is also affected by the chemical composition of the foaming solution, the interface mobility, the bubble size distribution, and many other factors [3–5]. A conventional approach to predict the liquid distribution within foam is to solve the drainage equation [4,6,7]. This requires known geometrical parameters of the foam, as well as information on the physicochemical properties of the solution [4,7,8]. The solution of the corresponding equation will yield the temporal and spatial evolution of the liquid fraction $\phi = V_l/V_f$, i.e., the ratio of liquid volume V_l to total foam volume V_f.

The drainage equation is based on the assumption of an isotropic foam structure with liquid flow occurring predominantly through Plateau borders. This does not always hold true. For instance, the contribution of the liquid transport through liquid films is still debated [9,10]. Drainage anisotropy in the foam has also been reported. Carrier and Colin [11] related the anisotropy to the difference in film thickness according to its spatial orientation. Exerted anisotropy might induce convective rolls [12] in a foam column, as shown by Heitkam and Eckert [13]. Neethling [14] elucidated a relation between the applied shear strain ε_{xy} to the foam and the horizontal deflection of a vertical drainage flow.

For instance, when small strain ε_{xy} is applied perpendicular to the direction of gravity y, the magnitude of the horizontal anisotropic flux q_a in the x direction follows a simple relation to the gravity-driven flux q_y:

$$q_a = 1/2 q_y \varepsilon_{xy}. \tag{1}$$

These predictions [14] have been based on numerical simulations of foam structure, performed with SURFACE EVOLVER software [15], and were hitherto not supported by experimental evidence. Hereinafter, the experimental evidence for the effect of shear on drainage anisotropy in liquid foam is provided. The paper is organized as follows: First, the details of the experimental installation and utilized measurement techniques are provided. Then, the results of liquid fraction measurements within the foam domain and its relation to shear deformations are presented. Finally, in the Discussion, the observed phenomena and their correlation to drainage anisotropy are characterized.

II. MATERIALS AND METHODS

A. Experimental setup

The experimental investigation focused on observation of liquid distribution within sheared and unchanged foams. The experimental setup for *in situ* neutron imaging experiments is shown in Fig. 1. The experiments were performed at measuring position 2 of the thermal neutron imaging beamline NEUTRA at the Paul Scherrer Institut [16]. After transmitting the sample the neutron beam hit a 30-μm-thick gadolinium oxysulfide scintillator, generating visible light that

*artem.skrypnik@tu-dresden.de
†sascha.heitkam@tu-dresen.de

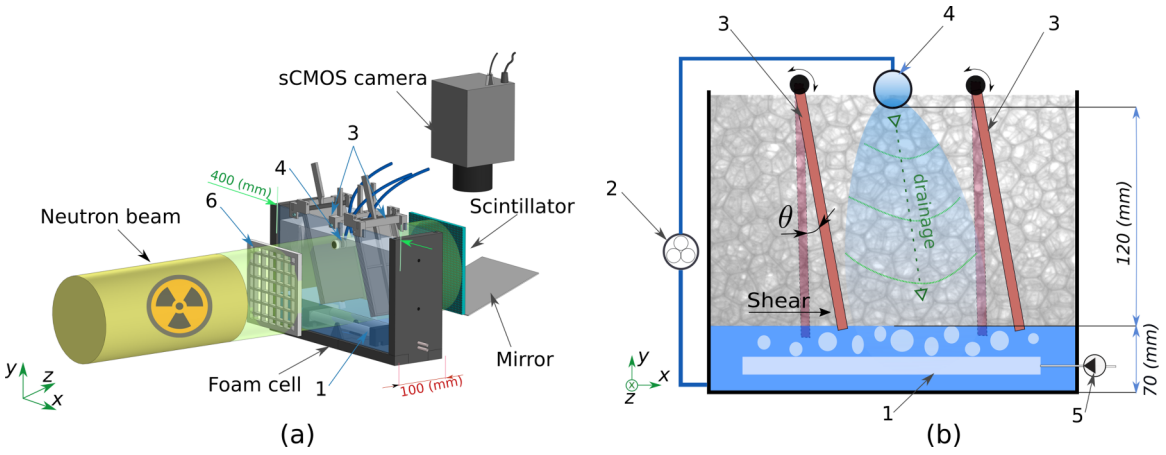

FIG. 1. The arrangement of the measurement setup (a) and a schematic of the foam cell with its component parts (b): 1, the bubble generator; 2, the peristaltic pump; 3, shearing plates, inclined by angle θ; 4, the drainage liquid source; 5, the air pump; 6, blackbody mesh.

was captured by a scientific complementary metal-oxide semiconductor (sCMOS) camera (Hamamatsu ORCA 4.0 v2). The pixel size of the generated images and the corresponding field of view (FOV) were equal to 59.8 μm and 120 × 120 mm, respectively [16]. The signal recorded by the camera corresponds to the number of neutrons impinging the scintillator and, thus, the camera exposure time. We set the exposure time to be 10 s within the scope of all the experiments, yielding the required signal magnitude.

Foam was generated in a rectangular cell manufactured by three-dimensional (3D) printing from polylactic acid, which includes 5-mm-thick glass plates of 400 mm width and 250 mm height separated by a distance of 100 mm. A surfactant solution of deionized water and dissolved sodium dodecyl sulfate (SDS, 6 g/L) was poured into the foam cell, providing a liquid filling level of $h_s \approx 67$ mm relative to the base of the cell.

Foam of different bubble sizes and polydispersities was used. The foam was produced from air with approximately 5×10^{-3} mol per liter of perfluorohexane (C_6F_{14}). Perfluorohexane slows down the foam coalescence significantly [17]. The air mixture was pumped through a porous tube or a tube with an orifice, which were submerged in a foaming solution and fixed at the bottom of the cell. The airflow rate Q_{air} was kept constant by a diaphragm vacuum pump (Laboport N 86 KN.18) and was equal to 6.0 L/min. We varied the bubble size by utilizing two different high-density polyethylene porous tubes of 19 mm inner diameter and 3.2 mm wall thickness, with pore sizes of 100 and 250 μm (Reichelt), and a tube with uniformly spaced 20 orifices of diameter $d_o = 0.8$ mm.

The Sauter mean diameter D_{32} and their related statistical parameters were evaluated by extracting a small volume of foam from the bulk, which then was placed between two thin glass plates spaced by $z = 1$ mm. The area of the squeezed bubbles A_b and their volume $V_b = Az$ were used to estimate the equivalent bubble diameter, $D = \sqrt[3]{6/\pi V_b}$, and Sauter mean diameter D_{32}. The standard deviation of the bubble diameter D was utilized as a measure for the bubble size polydispersity p. The corresponding measurement results are listed in Table I.

The overall amount of liquid was kept constant throughout all experiments. We extracted surfactant solution from the bottom of the cell and constantly returned it to the top of the cell with a Watson Marlow 323 DU peristaltic pump. To ensure the uniform flow distribution of the surfactant solution along the cell width (z direction, Fig. 1), a porous tube of 19 mm outer diameter was used to distribute the water. The tube was located at the center of the foam cell and filled the full width of the cell, $S_c = 100$ mm. The vertical distance between the water surface at the cell bottom and the drainage tube at its top was 110 mm. The corresponding drainage flow rates were $Q_w = 32$, 53, and 107 mL/min.

During the experiments the foam was subjected to shear. The shear was imposed by two vertical plates, which were mounted perpendicular to the neutron beam path. The plates were able to rotate together in parallel, to shear the foam sandwiched between the plates. The axis of rotation of the plates was at the cell top.

B. Experimental procedure

The foam was sheared by varying the angle of plate inclination (see Fig. 2). For each shear angle an individual neutron imaging experiment was performed, using the following procedure.

(1) The shearing plates were preliminarily inclined by angle θ to the left of vertical [Fig. 2(a)] providing the desired magnitude of strain

$$\varepsilon = \tan\theta. \tag{2}$$

TABLE I. Bubble and foam properties for the three different bubble generators employed. OF tube, tube with an orifice; PE tube, polyethylene porous tube.

Bubble generator	Bubble diameter D_{32} (mm)	Polydispersity (%)
PE tube (100-μm pore)	1.9	25
PE tube (250-μm pore)	2.8	17
OF tube (0.8-mm orifice)	4.7	16

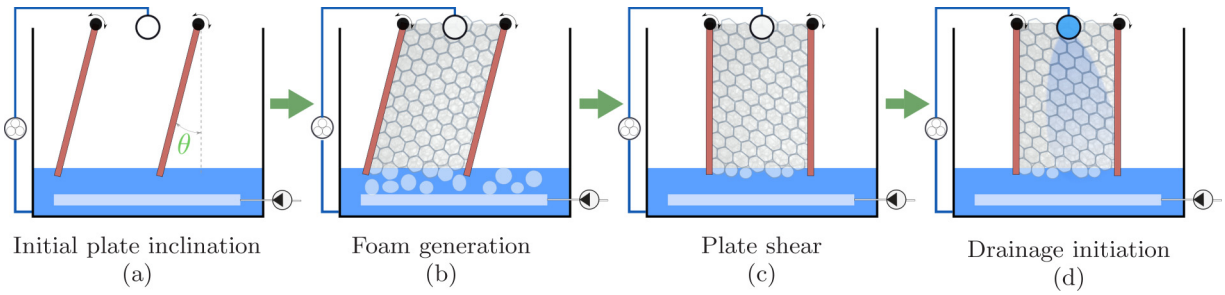

FIG. 2. [(a)–(d)] Schematic of the sequence of the experimental procedure. The line of sight is in the direction of the neutron beam.

(2) Fresh foam was generated to fill the interplate spacing [Fig. 2(b)]. The volume of generated foam exceeded the cell volume, providing a foam layer 8–10 cm in thickness on top of the cell.

(3) The plates then were sheared from left to right in the image plane [Fig. 2(c)] to be vertically aligned. Thus a strain of ε was imposed on the foam volume.

(4) Drainage flow was initiated on the lowest flow rate value [Fig. 2(d)].

(5) After waiting for 2 min, the image acquisition was started. We recorded ten images for each experimental run, which provided the required statistical information and resulted in 100 s total measurement time.

(6) The drainage flow rate was increased to the next value, and point (5) was repeated.

(7) After performing all targeted flow rates, the foam was completely removed from the cell. The next shear angle θ was set, continuing with a repeat of this procedure from point (1).

The foam was produced between inclined plates, which were shifted to a vertical position only after foam production. In that way, the shear due to the inclination of the plates during foam formation was captured in the foam structure while the foam was confined between the vertical plates. Thus the vertical plates did not influence the drainage flow as inclined plates would have done. This approach also prevents a possible initiation of convective rolls, similar to the tilting of the foam column under forced drainage [12].

C. Local strain and stress field determination

In order to evaluate the strain and the stress fields after foam shearing [Fig. 2(c)], we examined the rearrangement of the Plateau borders optically observing the process of foam generation and shearing. The arrangement of Plateau borders at the surface of the cell was tracked using a combination of back and front lights and a camera (Dalsa Genie Nano, M1930). The texture tensor M_{ij} and the stress tensor σ_{ij} were used to characterize the local state of the sheared foam [18–20]. The image processing for the texture and stress tensors is depicted in Fig. 3.

The texture tensor M_{ij} characterizes the current state of the network structure including its local elongation, compression, and structural anisotropy [19,20]. It is defined as the tensorial product of link vectors $\vec{l}$ averaged over the chosen interrogation window (IW):

$$M_{ij} = \langle l_i l_j \rangle. \tag{3}$$

The link vector $\vec{l}$ with its components (l_i, l_j) shall represent the structural element of the studied network [20]. In the case of liquid foam a vector linking the centers of the neighboring bubbles was used. The texture tensor is illustrated by an ellipse, where the semiaxes point in the direction of the eigenvectors and have the length of the corresponding eigenvalues of the texture tensor [19]. The major semiaxis [dotted line in Fig. 3(c)] corresponds to the direction of pattern elongation.

The stress tensor σ_{ij} corresponds to the line tension λ exerted by each Plateau border, which could be represented as vector quantity $\vec{m} = (m_i, m_j)$. The components of the stress tensor are defined by the averaging over the interrogation window

$$\sigma_{ij} = \lambda \rho \langle (m_i m_j / |m|) \rangle, \tag{4}$$

where the line tension λ was approximated by assuming that the average bubble film size oriented perpendicular to the wall $h = \langle m \rangle$. This yields $\lambda = 2\gamma h$ with corresponding foam surface tension γ. The number of Plateau borders per area of

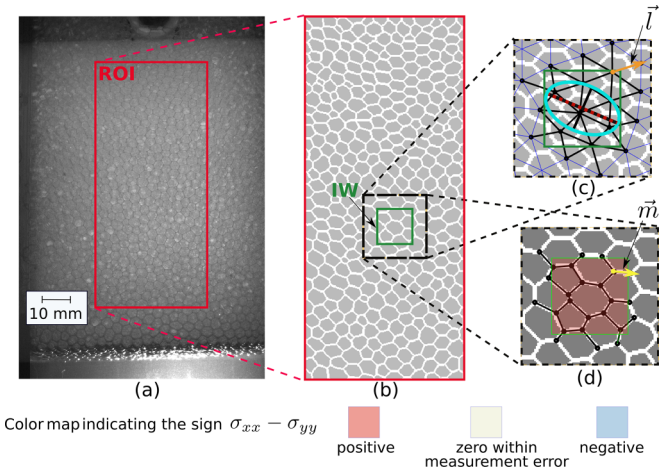

FIG. 3. Schematic sequence of the method to determine the local texture and stress tensors. The digital image of the foam structure (a) is postprocessed to extract the structural elements of foam—Plateau borders and bubbles (b)—within the region of interest (ROI). For an interrogation window (IW), vectors $\vec{l}$ connecting the bubble centers (c) were used to calculate a texture tensor M [Eq. (3)], while the stress tensor σ [Eq. (4)] was determined with the vectors $\vec{m}$ representing Plateau borders. The semiaxes of the ellipse (c) are proportional to the eigenvectors of the texture tensor M, and the color of the filled rectangle (d) corresponds to the sign of the normal stress difference (see key at bottom of figure).

interrogation window is noted as ρ, a number density. The sign of the normal stress difference $\sigma_{xx} - \sigma_{yy}$ is plotted as color in Fig. 3(d). Red and blue colors correspond to positive and negative values, respectively. White color corresponds to a maximal stress magnitude of zero (within 5% measurement uncertainty).

The foam structure was estimated for an ROI of size 40×75 mm^2 in the middle of the acquired image [Fig. 3(a)]. The image preprocessing by artificial neural networks [21,22] applicable for cellular structures resulted in segmented bubbles separated by Plateau borders of the foam. An initial image was split into small interrogation windows of 50×50 pixel^2 $\approx 9 \times 9$ mm^2 size, which is bigger than a single bubble but much smaller than the cell domain. A 50% overlapping of interrogation windows was set.

D. Liquid fraction determination

The magnitude of the local liquid fraction ϕ of foam was the pivotal parameter of this work. It was defined as the ratio of the equivalent liquid film thickness s_w between the glass plates along the z direction to the known thickness of the foam cell $s_c = 100$ mm, as

$$\phi = s_w / s_c. \tag{5}$$

The thickness of the equivalent liquid film s_w was estimated by means of neutron radiography. The transmittance of the incident beam flux I_0 of thermal neutrons along the path z [Fig. 1(a)] through the studied object was measured. It is related to the material composition of the object in the beam path. For a material consisting of j elements with their referring attenuation cross section σ_{a_j} and number density N_j the transmitted beam flux I results from the Beer-Lambert law [23] and equals

$$I = I_0 \exp\left(\int -\sum_j \sigma_{a_j} N_j(z) dz\right). \tag{6}$$

The attenuation from the gas phase in the foam is neglected, due to the low number density. Thus the amount of liquid s_w in the beam direction can be estimated with a simplified model

$$I = I_0 \exp\left(-\mu s_w\right), \tag{7}$$

known as Beer-Lambert's law [23], with the parameter μ denoting the linear neutron attenuation coefficient of the liquid. The influence of the minor components of foam (perfluorohexane and surfactants) has been neglected. Furthermore, the low SDS concentration in the solution leads to the assumption that the foaming solution consists of pure water, with an attenuation coefficient magnitude of $\mu = 3.6$ cm^{-1} [24].

The beam fluxes I_0 and I were determined by relating images recorded for the empty and foam-filled cells. The influence of scattered neutrons was compensated by the blackbody correction [24]. The dark current was measured by recording camera images with the neutron beam fully blocked. More details on the liquid fraction determination in foams are given by Heitkam *et al.* [25].

The measurements yielded a two-dimensional distribution of the liquid fraction ϕ. The foam cell was placed perpendicular to the beam path, such that neutrons transmitted the cell thickness of 100 mm between the glass plates. Since the porous drainage tube (Fig. 1) occupied the whole thickness of the cell, we assumed that the foam contained a uniform liquid distribution in the beam direction. Homogeneity of the liquid input along the dimension of the cell between the glass plates [Fig. 1(a)] could not be measured directly within the experiments and thus requires additional investigation, e.g., by means of positron emission tomography or x-ray synchrotron tomography, which might produce a 3D distribution of the liquid with high spatial and temporal resolution [26,27].

TABLE II. The variation of the reference liquid fraction ϕ_{ref} as a function of drainage flow rate Q_w and bubble size D_{32}.

	ϕ_{ref} (%)		
Q_w (mL/min)	$D_{32} = 1.9$ mm	$D_{32} = 2.8$ mm	$D_{32} = 4.7$ mm
32	0.65	0.38	0.16
54	0.98	0.61	0.19
107	1.63	1.05	0.46

This approach for estimating the liquid fraction was validated by estimating the thickness of a glass wedge filled with a surfactant solution. The wedge thickness varies over the range 0–5 mm, to emulate liquid fraction values between 0 and 5%. The relative deviation between the estimated and actual wedge thicknesses was within an acceptable range of $\pm 10\%$ [28].

We have defined reference values for the liquid fraction within the cell, denoted as ϕ_{ref}, which can be found in Table II. These reference values are determined as the amplitudes of Gaussian functions [refer to Eq. (8)] fitted to the liquid fraction distribution within the central region of the cell below the drainage input, specifically at line 1 in Fig. 4(a). These reference values are obtained through multiple experimental runs conducted for the respective drainage flow rates Q_w and bubble sizes D_{32}.

E. Measurement of drainage deflection

The experiments were carried out under steady-state conditions. The time that draining liquid needed to reach the bottom of the cell was estimated separately, by observing the propagation of the drainage front, and equalled approximately 3 s. The delay time before image acquisition was 2 min, which is considerably larger and is sufficient to achieve a steady-state liquid distribution.

The drainage flow input was located in the center of the field of view, as shown in Fig. 4(a). It is expected that for a stress-free foam the liquid distribution would be symmetrical with respect to the point of the drainage input x_0 along the horizontal axis x. Herewith, the maximum magnitude of the liquid fraction ϕ is in the center of the FOV, and the liquid fraction decreases as one approaches the left and right borders. As predicted by Neethling [14], an increase in shear of the foam would increase the rate of anisotropic drainage in the horizontal direction, deflecting the center of the drainage flow more and more to the right side yielding larger values for x. We tested this hypothesis by measuring the deflection of the drainage flow between consecutive height levels.

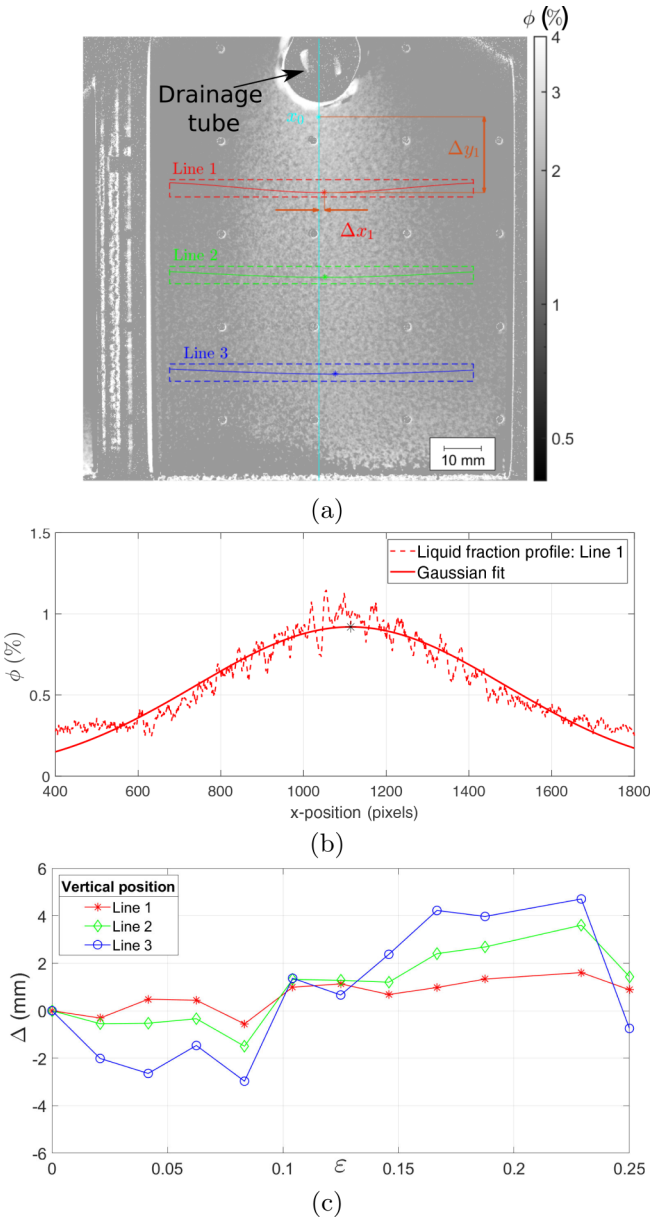

FIG. 4. An example of the process for determining liquid fraction deflection from image analysis: A Gaussian model [Eq. (8)] was fitted to a column-averaged liquid fraction distribution at three heights (dashed rectangles) of the 2D liquid fraction distribution (a). The corresponding Gaussian fits (the values are scaled) are depicted as solid lines in (a), and one is shown explicitly in (b) for line 1. The related absolute deflections Δx_i of the peak positions, relative to the initial drainage point x_0 [cyan line in (a)], and corresponding vertical distances Δy_i were then used to estimate the relative deflections Δ [Eq. (10)] as a function of the applied strain ε (c). The 2D liquid profile corresponds to the bubble diameter of $D_{32} = 2.8$ mm and drainage flow rate $Q_w = 107$ mL/min.

The center position of drainage flow was determined by applying a Gaussian fit to the liquid fraction distribution along the horizontal direction

$$\phi(x) = A \exp\left[-\left(\frac{x - x_{\text{peak}}}{c_1}\right)^2\right], \tag{8}$$

with A being the amplitude of the peak value, x_{peak} being its central position, and c_1 being the width of the distribution. To reduce noise in the liquid fraction data, $\phi(x)$ was averaged over 80 pixels in the vertical direction as marked in Fig. 4(a).

The peak position x_{peak} of the Gaussian fit was taken as the indicator of the horizontal center of the drainage flow at the corresponding vertical position. Figure 4(a) shows the Gaussian fits (equally scaled) for three lines at different positions down the drainage tube in the cell. Figure 4(b) shows the corresponding liquid fraction profile and Gaussian fit [Eq. (8)] for one position. The drainage injection point x_0 for each experimental run was determined in a similar fashion, performing a Gaussian fit just underneath the drainage injection tube. For better precision, two fits in slightly different regions were performed, and the resulting values of x_0 were averaged.

The absolute deflection of the draining flow profile at the ith height level was determined as

$$\Delta x_i^{\{\varepsilon\}} = x_{\text{peak}_i}^{\{\varepsilon\}} - x_0^{\{\varepsilon\}}. \tag{9}$$

The relative deflection was estimated by subtracting the corresponding deflection values at zero shear, $\varepsilon = 0$:

$$\Delta_i^{\{\varepsilon\}} = \Delta x_i^{\{\varepsilon\}} - \Delta x_i^{\{\varepsilon=0\}}. \tag{10}$$

Figure 4(c) shows exemplarily the deflection Δ_i in relation to the applied shear for the foam with average bubble size $D_{32} = 2.8$ mm and drainage flow of $Q_w = 107$ mL/min. The normalized deflection δ_i value was determined in order to quantify the correlation between the imposed strain ε and observed flow anisotropy, as

$$\delta_i = \Delta_i^{\{\varepsilon\}} / \Delta y_i, \tag{11}$$

which is the ratio of deflection Δ_i at the ith image pixel array to the corresponding vertical distance Δy_i to the position of the drainage input [Fig. 4(a)].

Following the hypothesis of Ref. [14] given in Eq. (1), the normalized deflection δ would be proportional to the strain amplitude ε, i.e.,

$$\delta = k\varepsilon, \quad \text{with } k = 0.5, \tag{12}$$

where k is the proportionality between δ and ε.

III. RESULTS

We estimated the deflection of a drainage flow according to Eq. (11) for the variations in drainage flow rate Q_w, yielding liquid fraction modulations (Fig. 5).

Examination of the obtained results reveals a distinct trend: the values of the normalized deflection δ increase with applied strain. The increasing values of δ are qualitatively in line with the expected deflection of the drainage flow predicted by Neethling [14]. The normalized deflections at different heights in the foam cell [Fig. 4(a)] collapse reasonably well onto a single curve, as the deflections are normalized by the corresponding vertical distance Δy. As the liquid fraction increases, the deflection of drainage flow becomes less prominent. For instance, for foam with an average bubble size of $D_{32} = 4.7$ mm the slope k of deflection lines decreases from $k = 0.38$ to $k = 0.28$, and then to $k = 0.22$, as the flow rate magnitude increases from $Q_w = 32$ mL/min to

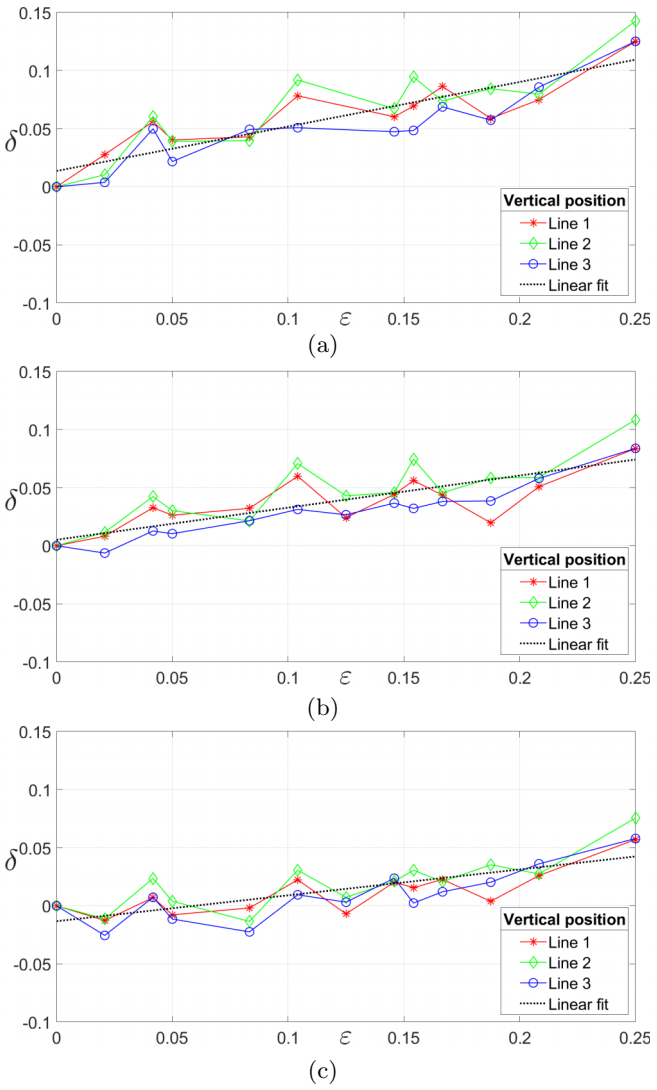

FIG. 5. The effect of the liquid fraction on the deflection δ of a draining liquid and imposed strain ε: (a) $Q_w = 32$ mL/min, (b) $Q_w = 53$ mL/min, and (c) $Q_w = 107$ mL/min, with constant bubble size $D_{32} = 4.7$ mm.

$Q_w = 53$ mL/min and then to $Q_w = 107$ mL/min, respectively.

Additionally, the observed behavior depends on the bubble size. Table III compares the relative deflections for different bubble generators, i.e., different D_{32}, and different flow rates. For the foam with the smallest average bubble diameter of $D_{32} = 1.9$ mm the correlation for the drainage deflection was not observed ($k \approx 0$) for any flow rate.

TABLE III. The magnitude of the slope k for different Sauter diameters D_{32} and drainage liquid flow rates Q_w. The standard error of the estimate is given in parentheses.

	k		
Q_w (mL/min)	$D_{32} = 4.7$ mm	$D_{32} = 2.8$ mm	$D_{32} = 1.9$ mm
32	0.38 (0.04)	0.48 (0.08)	0.05 (0.11)
53	0.28 (0.03)	0.42 (0.07)	−0.05 (0.09)
107	0.22 (0.03)	0.34 (0.06)	0.01 (0.05)

Figure 6 visualizes the texture tensor M [Eq. (3)] and the stress tensor σ [Eq. (4)], for foam with $D_{32} = 4.7$ mm and a drainage flow rate of $Q_w = 32$ mL/min, resulting from the increasing strain ε of the foam cell. A nonhomogeneous distribution of the stresses within the foam (leftmost panel in Fig. 6) is present even at zero imposed strain $\varepsilon = 0$. Comparing $\varepsilon = 0.2$ and $\varepsilon = 0.3$, the measured strain distribution in the foam does not change significantly. It is important to note that Fig. 6 plots the stress distribution at the transparent side wall, which might differ significantly from the stress distribution in the bulk, due to friction stress at the wet side wall. Similar effects have been revealed by Katgert *et al.* [29]. Also, these optical measurements were performed not simultaneously with the neutron radiography, but in a subsequent reproduction of the experiment. Thus Fig. 6 should only be considered as an illustration of the stress distribution rather than a precise measurement of the bulk stress distribution.

IV. DISCUSSION

We do see an increased deflection of the vertical drainage with increasing strain amplitude. However, the magnitude of the deflection of the drainage flow is significantly lower than that predicted by Neethling [14]. In the case of shear being imposed perpendicular to the direction of gravity it was proposed that anisotropic flow q_{anis} is related to a flow in the direction of gravity force q_y as follows from Eqs. (1) and (12) [14]. This would result in values of $k = 0.5$ for the horizontal deflection. However, we measured maximum values for k of 0.48. With decreasing bubble size, increasing polydispersity, and increasing liquid fraction, k further decreased. Neethling developed the corresponding numerical predictions for a perfectly dry, monodisperse foam [14]. Such assumptions could not be applied to the liquid foam utilized in these experimental measurements. The measured liquid fraction within the ROI was in the range $\phi_{\text{ref}} = 0.5$–1.6% (Table II) for all the bubble diameters and drainage liquid supply. In addition, the assumption of monodispersed bubbles did not hold, as shown in Table I.

Additionally, the theory proposed by Neethling [14] is only valid up until the point at which the foam starts to yield, which is characterized by topological changes in the foam. The topological changes reduce the amount of structural anisotropy that a given amount of shear induces. These topological changes will occur more readily in foams that have higher liquid contents [30,31]. As demonstrated in Fig. 5 the drainage deflection is lower for foams with higher liquid fractions. However, the applied liquid fractions are very small (see Table II), i.e., well below the jamming point, and should not completely erase anisotropy.

In addition, the dependency of drainage anisotropy on the bubble size (Table III) could be explained by the higher level of polydispersity (see Table I), which is also reported to reduce the yield strain [32].

Analysis of the texture tensor M maps (Fig. 6) reveals that even at zero imposed strain $\varepsilon = 0$ there is prominent anisotropy in stress and the foam structure. This agrees

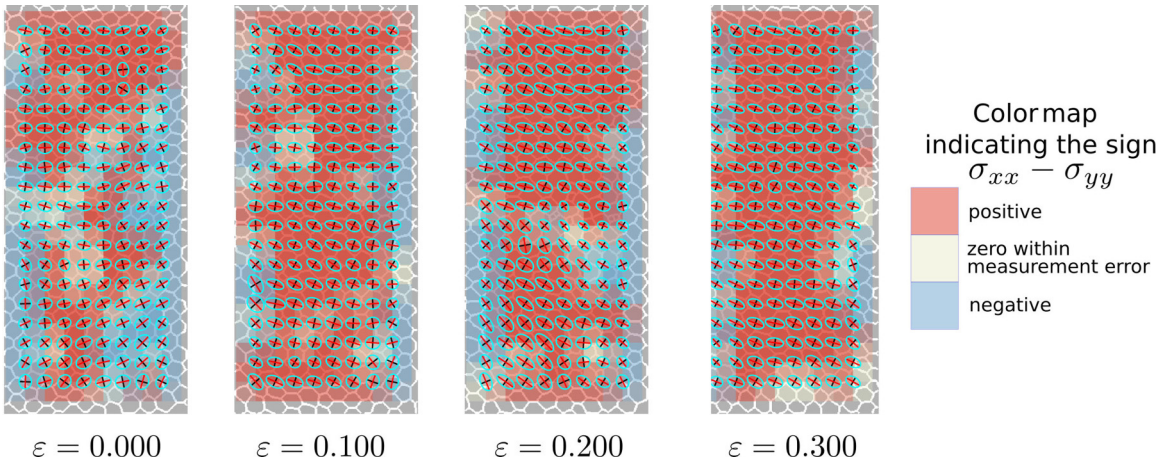

FIG. 6. Estimated texture tensor M maps for different magnitudes of the global strain ε, which are colored according to the sign of the normal stress difference $\sigma_{xx} - \sigma_{yy}$ (foam bubble size $D_{32} = 4.7$ mm, and drainage flow rate $Q_w = 32$ mL/min).

with our observations of a systematic deflection in the drainage flow at zero imposed strain $\varepsilon = 0$. This deflection is superimposed with the deflection from the applied strain. Potentially, due to the foam generation processes, local stresses could be accumulated in the foam structure. For example, during the foam generation process, foam flows through the void between the inclined plates, making the foam slightly compressed. Also, the cylinder-shaped drainage tube at the top of the cell acts as an obstacle to the foam flow. These changes to the geometry of the flow path might result in accumulated stresses within the bulk foam, thereby locally straining the foam and affecting further measurements. The initial anisotropy in the liquid fraction distribution thus was included during the deflection field estimation in Eq. (10) for the relative deflection. With increasing shear angle, the distribution of stress and structure anisotropy becomes more homogeneous over the foam column (Fig. 6). Presumably, at shear angles above 0.2, yielding occurred, maintaining the resulting stress homogeneously near the yielding limit. This might explain why in Fig. 4(c) the deflection δ does not increase for higher shear angles.

Despite all these factors which potentially affected the measurements, we have demonstrated a deflection of vertical drainage that is correlated with the imposed strain. This proves the presence of drainage liquid anisotropy in the foam. Even at zero imposed strain an initial strain of the foam structure was identified that influenced the drainage distribution inside the foam. This demonstrates the relevance of anisotropic drainage for any foam drainage experiment. Significant effort has to be taken to generate a foam that is free of stress.

V. CONCLUSION

The distribution of draining liquid in a sheared foam was studied by means of neutron radiography. A horizontal deflection of the vertical drainage was found that grows with increasing shear angle. This is a direct experimental proof of the phenomenon of anisotropic drainage, predicted by Neethling [14]. The maximal deflection was close to the prediction of Neethling [14]. However, for smaller bubbles and higher liquid fractions, the deflection was smaller or even vanished.

The occurrence of anisotropic drainage has implications for designing forced-drainage experiments, as initial stress from the foam generation process might cause inhomogeneous liquid fraction distributions or even convection rolls within the foam [13].

Further investigations could be dedicated to the three-dimensional characterization of the anisotropic drainage, which requires foam tomography studies, for instance, by means of x-ray or neutron tomography or by positron emission tomography.

ACKNOWLEDGMENTS

Financial support from the German Research Foundation Grant No. HE 7529/3-1 (431077191) is gratefully acknowledged. This work is based on experiments performed at the Swiss spallation neutron source SINQ, Paul Scherrer Institut, Villigen, Switzerland.

[1] B. Dollet and C. Raufaste, Rheology of aqueous foams, C. R. Phys. **15**, 731 (2014).

[2] R. Höhler and S. Cohen-Addad, Rheology of liquid foam, J. Phys.: Condens. Matter **17**, R1041 (2005).

[3] A. Saint-Jalmes, Physical chemistry in foam drainage and coarsening, Soft Matter **2**, 836 (2006).

[4] S. A. Köhler, S. Hilgenfeldt, and H. A. Stone, A generalized view of foam drainage: Experiment and theory, Langmuir **16**, 6327 (2000).

[5] M. Safouane, M. Durand, A. Saint Jalmes, D. Langevin, and V. Bergeron, Aqueous foam drainage. Role of the rheology of the foaming fluid, J. Phys. IV **11**, Pr6-275 (2001).

[6] G. Verbist, D. Weaire, and A. M. Kraynik, The foam drainage equation, J. Phys.: Condens. Matter **8**, 3715 (1996).
[7] S. Hutzler, S. Cox, and G. Wang, Foam drainage in two dimensions, Colloids Surf. A: Physicochem. Eng. **263**, 178 (2005).
[8] S. A. Koehler, S. Hilgenfeldt, and H. A. Stone, Liquid flow through aqueous foams: The node-dominated foam drainage equation, Phys. Rev. Lett. **82**, 4232 (1999).
[9] V. Carrier, S. Destouesse, and A. Colin, Foam drainage: A film contribution? Phys. Rev. E **65**, 061404 (2002).
[10] S. Köhler, S. Hilgenfeldt, and H. Stone, Foam drainage on the microscale, J. Colloid Interface Sci. **276**, 420 (2004).
[11] V. Carrier and A. Colin, Anisotropy of draining foams, Langmuir **18**, 7564 (2002).
[12] S. Hutzler, S. J. Cox, E. Janiaud, and D. Weaire, Drainage induced convection rolls in foams, Colloids Surf. A: Physicochem. Eng. **309**, 33 (2007).
[13] S. Heitkam and K. Eckert, Convective instability in sheared foam, J. Fluid Mech. **911**, A54 (2021).
[14] S. J. Neethling, Effect of simple shear on liquid drainage within foams, Phys. Rev. E **73**, 061408 (2006).
[15] K. A. Brakke, The surface evolver, Exp. Math. **1**, 141 (1992).
[16] E. H. Lehmann, P. Vontobel, and L. Wiezel, Properties of the radiography facility NEUTRA at SINQ and its potential for use as European reference facility, Nondestr. Test. Eval. **16**, 191 (2001).
[17] K. Steck, M. Hamann, S. Andrieux, P. Muller, P. Kékicheff, C. Stubenrauch, and W. Drenckhan, Fluorocarbon vapors slow down coalescence in foams, Adv. Mater. Interfaces **8**, 2100723 (2021).
[18] G. K. Batchelor, The stress system in a suspension of force-free particles, J. Fluid Mech. **41**, 545 (1970).
[19] M. Asipauskas, M. Aubouy, J. A. Glazier, F. Graner, and Y. Jiang, A texture tensor to quantify deformations: the example of two-dimensional flowing foams, Granular Matter **5**, 71 (2003).
[20] F. Graner, B. Dollet, C. Raufaste, and P. Marmottant, Discrete rearranging disordered patterns, part I: Robust statistical tools in two or three dimensions, Eur. Phys. J. E **25**, 349 (2008).
[21] J. P. Vigueras-Guillen, J. van Rooij, A. Engel, H. G. Lemij, L. J. van Vliet, and K. A. Vermeer, Deep learning for assessing the corneal endothelium from specular microscopy images up to 1 year after ultrathin-DSAEK surgery, Transl. Vision Sci. Technol. **9**, 49 (2020).
[22] L. Knüpfer and S. Heitkam, A machine learning approach to determine bubble sizes in foam at a transparent wall, Meas. Sci. Technol. **33**, 067001 (2022).
[23] A. A. Harms and D. R. Wyman, *Mathematics and Physics of Neutron Radiography*, Reidel Texts in the Mathematical Sciences (Springer, New York, 1986), Vol. 1.
[24] C. Carminati, P. Boillat, F. Schmid, P. Vontobel, J. Hovind, M. L. Morgano, M. Raventos, M. Siegwart, D. Mannes, C. Gruenzweig, P. Trtik, E. Lehmann, M. Strobl, and A. Kaestner, Implementation and assessment of the black body bias correction in quantitative neutron imaging, PLoS One **14**, e0210300 (2019).
[25] S. Heitkam, M. Rudolph, T. Lappan, M. Sarma, S. Eckert, P. Trtik, E. Lehmann, P. Vontobel, and K. Eckert, Neutron imaging of froth structure and particle motion, Miner. Eng. **119**, 126 (2018).
[26] K. Cole, P. R. Brito-Parada, A. Morrison, I. Govender, A. Buffler, K. Hadler, and J. J. Cilliers, Using positron emission tomography (PET) to determine liquid content in overflowing foam, Chem. Eng. Res. Des. **94**, 721 (2015).
[27] A. Kastengren and C. F. Powell, Synchrotron x-ray techniques for fluid dynamics, Exp. Fluids **55**, 1686 (2014).
[28] M. Ziauddin, E. Schleicher, P. Trtik, L. Knüpfer, A. Skrypnik, T. Lappan, K. Eckert, and S. Heitkam, Comparing wire-mesh sensor with neutron radiography for measurement of liquid fraction in foam, J. Phys.: Condens. Matter **35**, 015101 (2022).
[29] G. Katgert, B. P. Tighe, M. E. Möbius, and M. van Hecke, Couette flow of two-dimensional foams, EPL (Europhys. Lett.) **90**, 54002 (2010).
[30] T. Mason, J. Bibette, and D. Weitz, Yielding and flow of monodisperse emulsions, J. Colloid Interface Sci. **179**, 439 (1996).
[31] A. Saint-Jalmes and D. J. Durian, Vanishing elasticity for wet foams: Equivalence with emulsions and role of polydispersity, J. Rheol. **43**, 1411 (1999).
[32] B. S. Gardiner, B. Z. Dlugogorski, and G. J. Jameson, The steady shear of three-dimensional wet polydisperse foams, J. Non-Newtonian Fluid Mech. **92**, 151 (2000).